Acta Metallurgica Sinica (English Letters) (2023) 36:439–455
https://doi.org/10.1007/s40195-022-01480-w

Mechanical and Corrosion Behavior of a Biomedical Mg–6Zn–0.5Zr Alloy Containing a Large Number of Twins

Chang-Jian Yan[1,7] · Bo Guan[2] · Yun-Chang Xin[2,3] · Ling-Yu Zhao[4] · Guang-Jie Huang[2] · Rui Hong[2] · Xiao-Bo Chen[5] · Paul K. Chu[6]

Received: 20 July 2022 / Revised: 31 August 2022 / Accepted: 12 September 2022 / Published online: 10 November 2022

Abstract
The strong texture of Mg alloys can lead to strong tension–compression yield asymmetry and corrosion anisotropy, and this will consequently affect the effectiveness of hard tissue implants. A biomedical Mg–6Zn–0.5Zr alloy containing a large number of $\{10\bar{1}2\}$ primary twins and $\{10\bar{1}2\}$–$\{10\bar{1}2\}$ secondary twins is successfully prepared by cross compression. The dual twin structure not only removes the tension–compression yield asymmetry completely, but effectively reduces the corrosion anisotropy without compromise of corrosion resistance. The difference between the largest corrosion rate and smallest one is ~ 1.2 times compared to ~ 1.6 times of the original materials. It is found that the reduced corrosion anisotropy is related to re-distribution of crystallographic orientations by twins.

Keywords Biomedical Mg alloy · Corrosion · Mechanical anisotropy · Texture · Twins

1 Introduction

Magnesium (Mg) alloys are biodegradable implant materials due to the favorable biocompatibility and absorbability [1]. In addition, Mg as an essential element in the human body [2] is involved in many metabolic reactions and biological mechanisms [3] which will promote the growth [4], proliferation [5], as well as differentiation of osteoblasts [6]. However, Mg alloys are susceptible to fast corrosion especially in the presence of chloride ions in the physiological environment [7]. Thus the careful control of the degradation rate is required to obviate the need for a second surgical process [8] as well as to alleviate patient trauma and reduce medical cost [9]. In fact, Mg alloys are more suitable for load-bearing applications than many common ceramics, biodegradable polymers, and metals because of the high mechanical strength as well as fracture toughness [10]. Furthermore, the elastic modulus of Mg alloys (41–45 GPa) is closer to that of natural bones (3–20 GPa) [11] consequently mitigating the stress shielding effect while accelerating bone healing [12].

Available online at http://link.springer.com/journal/40195.

✉ Chang-Jian Yan
cjyan@icost.ac.cn

✉ Yun-Chang Xin
ycxin@cqu.edu.cn

✉ Rui Hong
hongrui@cqu.edu.cn

[1] Institute of Corrosion Science and Technology, Guangdong 510070, China

[2] International Joint Laboratory for Light Alloys, College of Materials Science and Engineering, Chongqing University, Chongqing 400030, China

[3] Key Laboratory for Light-Weight Materials, Nanjing Tech University, Nanjing 210009, China

[4] School of Mechanical Engineering, Yangzhou University, Yangzhou 225127, China

[5] School of Engineering, RMIT University, Carlton 3053, VIC, Australia

[6] Department of Physics, Department of Materials Science & Engineering, Department of Biomedical Engineering, City University of Hong Kong, Tat Chee Avenue, Kowloon, Hong Kong, China

[7] Institute of Metal Research, Chinese Academy of Sciences, Shenyang 110016, China

Mechanical strength is one of the important properties of biomaterials [13]. Generally, the mechanical properties can be improved by plastic deformation such as extrusion [14], rolling [15], forging [16], equal channel angular pressing (ECAP) [17], high pressure torsion [18], and cyclic extrusion and compression [19]. However, the strong tension–compression yield asymmetry, in which the tensile yield strength is different from that of the compressive one, has been frequently observed from textured Mg alloys such as Mg–Zn–Ho alloys [20], Mg–2Zn–2Gd alloy [21], AZ31 alloy [22], AZ80 alloy [23], and AZ91 alloy [24]. For example, Xin et al. [25] have reported that the tensile yield strength along the rolling direction (RD) of a basal-textured Mg AZ31 plate is 148 MPa in comparison with a compressive yield strength of 67 MPa. The strong tension–compression yield asymmetry poses a strong challenge for the design and application of Mg alloys as orthopedic and dental implants.

The reason for the tension–compression yield asymmetry has been investigated, and it is related to the activation of $\{10\bar{1}2\}$ twinning. If $\{10\bar{1}2\}$ twinning is pre-dominated in the compression process, and the tension process is usually pre-dominated by prismatic slip [26]. The lower critical resolved shear stress (CRSS) of $\{10\bar{1}2\}$ twinning compared to prismatic slip will leads to the difference between the tension and compression yield strength [27]. It has been shown that the tension–compression yield asymmetry can be reduced by texture tailoring [25], grain refinement [28], and precipitation [29]. The main mechanism for the reduced tension–compression asymmetry involves balancing the activities of slips and $\{10\bar{1}2\}$ twinning [30]. However, there have been few investigations focus on the tension–compression yield asymmetry of biomedical Mg alloys. Human bones such as the femur, tibia, and hip are subjected to tension and compression during motion and so how to reduce the tension–compression asymmetry of Mg alloys must be considered. Besides the tension–compression yield asymmetry, a strong texture also can generate corrosion anisotropy in the Mg alloys. For example, Song et al. [31] reported that the corrosion rate of a cross-sectional surface of the rolled AZ31 alloy with a large concentration of $\{10\bar{1}0\}$ and $\{10\bar{1}2\}$ prism planes was 8 times larger than that of a rolled surface composed of the {0002} basal planes in the 5% NaCl solution. Jiang et al. [[32]] also found that the corrosion rates of the AZ80 alloy in 3.5% NaCl rose with decreased {0002} plane intensity and increased $\{10\bar{1}0\}$ and $\{2\bar{1}\bar{1}0\}$ planes intensities. But, till now, how to reduce the corrosion anisotropy in Mg biomaterials with strong crystallographic texture is rarely investigated. Therefore, a reduction of both the mechanical and corrosion anisotropy is crucial to clinical implementation of biomedical Mg alloys.

Mg–Zn-based alloys are promising biomedical implants because they are not only the second strongest ductile alloy system [33], but possess greatly reduced corrosion rates [34]. There are mainly two types of alloy elements in ZK60 alloy, Zn and Zr. Zn is an essential element in the human body and plays important roles in many biological processes [35]. Zr has been proven to be biologically compatible [36]. ZK60 alloy exhibited good in vitro and in vivo degradation rates, as well as excellent biocompatibility [37]. ZK60 alloy exhibits good mechanical properties with a uniform elongation of 10%–30% and an ultimate tensile strength of 200–400 MPa after suitable plastic processing regimes, such as hot rolling [33], ECAP [38], which make it a desirable candidate as an bone implants. In the work described here, a dual twin structure composed of the $\{10\bar{1}2\}$ primary twin and $\{10\bar{1}2\}$–$\{10\bar{1}2\}$ secondary twin is prepared by cross compression along the transverse direction (TD) and rolling direction (RD) of the hot-rolled Mg–6Zn–0.5Zr alloy for biomedical implants. A nearly removed tension–compression yield asymmetry and significantly reduced corrosion anisotropy is found in this study. The corresponding mechanism for such reduced mechanical and corrosion anisotropy is also systematically studied and discussed.

2 Experimental

2.1 Thermomechanical Processing and Mechanical Tests

The hot-rolled Mg–6Zn–0.5Zr alloy (25 mm thick) was annealed at 400 ℃ for 24 h and quenched in water at room temperature. After the solid solution treatment, it was cut into blocks with dimensions of 30 mm (transverse direction, TD) × 30 mm (rolling direction, RD) × 25 mm (normal direction, ND) for the pre-deformation process illustrated schematically in Fig. 1. The strain rate of pre-deformation is 0.001 s^{-1}. The dual twin structure was prepared by constant 2.5% pre-deformation along the RD and 2.5%

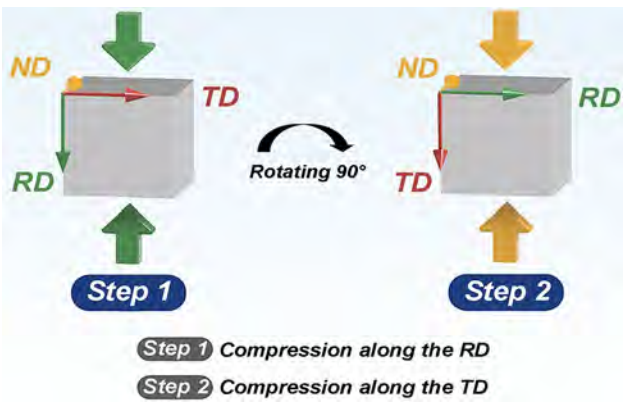

Fig. 1 Schematic diagram of the pre-deformation process

pre-deformation along the TD at room temperature. Graphite was used to reduce the friction between the holder and sample. The samples subjected to the solid solution treatment and pre-deformation were aged at 180 ºC in a silicone oil bath. The age hardening response as a function of time was assessed on the Vickers hardness theater. The solid solution treatment materials processed under peak-aged conditions was designated as STA sample and pre-deformed materials processed under peak-aged conditions was denoted as PDA sample.

The mechanical properties of the STA and PDA samples were determined under tension and compression along the ND, RD, and TD at room temperature at a strain rate of 0.001 s^{-1}. The samples with a size of 8 mm × 7 mm × 7 mm for compression and a dog-bone-shaped samples with the nominal gage dimensions of 25 mm × 4 mm × 1.7 mm for tension along the ND, RD, and TD. Each test was repeated three times. The samples for the corrosion assessment of the surface perpendicular to the ND, RD, and TD were also designated as plane RD-TD, plane ND-TD, and plane ND-RD, respectively.

2.2 Microstructure examination

Electron backscattering diffraction (EBSD) was conducted on a scanning electron microscope (SEM, TESCAN MIRA 3 and Zeiss Auriga SEM–FIB) equipped with the HKL-electron backscattered diffraction system and quasi in situ EBSD mapping was carried out to study the deformation behavior of the PDA sample. The fractions of the primary twins or secondary twins were calculated using the area fraction via CHANNEL 5. In the measurement, the sample was measured, reloaded outside the SEM, and then re-measured at the same region using a step size of 0.5–0.8 µm. The samples for EBSD mapping were mechanically ground to 2000# and electrochemical polished in the AC2 electrolyte. Studies have reported that upon severe annealing the process of secondary recrystallization proceeds until a homogeneous texture is achieved throughout the thickness [39]. In this study, the middle surface of the sample after annealed at 400 ºC for 24 h was selected for the XRD test. The data were analyzed by the CHANNEL 5 software and the pole figures were determined by X-ray diffraction (XRD, Rigaku D/max-2500PC).

The thin foil specimens for scanning transmission electron microscopy (STEM) were prepared by mechanical polishing from 500 to 60–80 µm. They were punched into 3 mm diameter disks and ion-milled using the Gatan PIPS 695 at about −70 ºC. The 5 keV ion beam impinged the specimen at an angle of 6º to form a hole and then the angle and beam energy were reduced gradually to 3º and 3 keV, 2º and 2 keV, and 2º and 1 keV sequentially to flatten the surface. STEM was carried out on the FEI Tecnai G^2 F20 at 200 kV.

2.3 Corrosion Tests

Hank's solution containing the Hank's balanced salt (composed of 8.0 g/L NaCl, 0.4 g/L KCl, 0.14 g/L $CaCl_2$, 0.1 g/L $MgCl_2{\cdot}6H_2O$, 0.15 g/L $Na_2HPO_4{\cdot}12H_2O$, 0.06 g/L KH_2PO_4, 0.1 g/L $MgSO_4{\cdot}7H_2O$) and distilled water was used and NaOH and sodium bicarbonate were employed to adjust the pH. The samples were ground with 4000# water proof diamond paper, cleaned ultrasonically with alcohol, and dried with air before the immersion test. The corrosion rate was determined by the hydrogen evolution method schematically illustrated in Fig. 2. In Fig. 2, the tested sample is marked in blue color. When the samples were immersed in the Hank's solution, the following reaction occurred:

$$Mg + 2H_2O \rightarrow Mg^{2+} + 2OH^- + H_2 \rightarrow Mg(OH)_2 + H_2.$$

In the reaction, the amount of dissolved magnesium was calculated from the volume of hydrogen generated. The hydrogen volume was collected through the drainage method using measuring cylinder. To measure the corrosion anisotropy, the corrosion rates of the plane RD-TD, plane ND-TD, and plane ND-RD were measured in each test, four samples were assessed by collecting the evolved hydrogen in 600 ml of Hank's solution at 25 ºC. Each test was repeated two times and the volume of emitted hydrogen was monitored as a function of immersion time. The corrosion morphology of

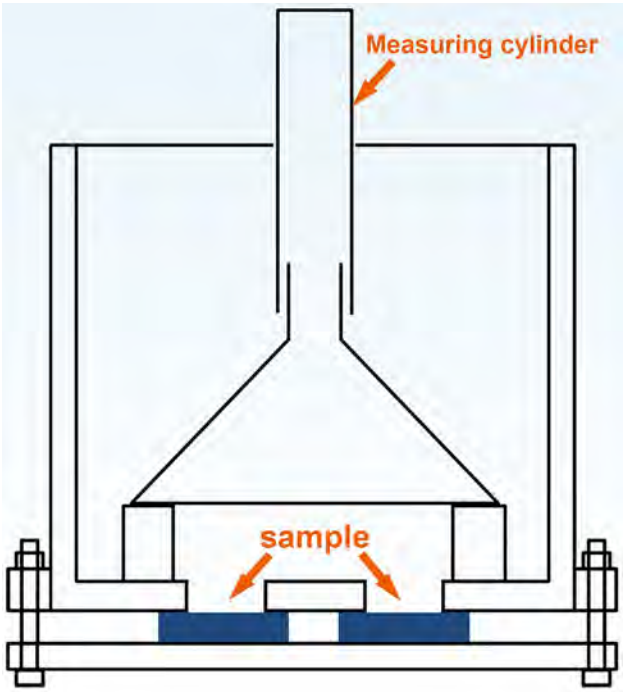

Fig. 2 Schematic illustration of the hydrogen evolution method

samples after immersion for 6, 24 or 72 h was examined by scanning electron microscopy (SEM, TESCAN VEGA 3 LMH).

The electrochemical tests were conducted using a three-electrode cell with a Gamry reference 600 + Pt sheet as the measuring electrode, calomel electrode as the reference electrode, and the sample with an exposed area of 1 cm^2 as the working electrode. The electrochemical experiments were carried out at room temperature in glass cells containing 200 ml of the solution. 10 and 1 mV/s scanning rates were used in the open circuit potential (OCP) and polarization tests, respectively. The impedance data were recorded from 100 kHz to 10 mHz with a 10 mV sinusoidal perturbation signal at the open circuit potential. The equivalent circuits (EC) were constructed to analyze the EIS spectra which were fitted with the ZSimpWin software.

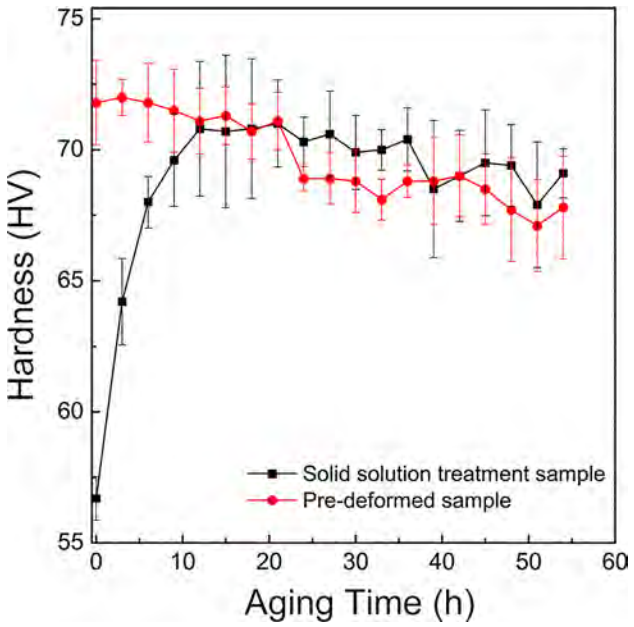

Fig. 3 Age-hardening curves of the solid solution treatment sample and pre-deformed sample

3 Results

3.1 Hardness

Figure 3 shows the hardness curves of the solid solution treatment sample and pre-deformed sample during isothermal ageing treatment at 180 ℃. Before aging treatment, the hardness values of the solid solution treatment sample and pre-deformed sample are quite different, which are 56.7 and 71.8 HV, respectively. The hardness of the solid solution treatment sample is enhanced rapidly to a value of 70.8 HV after 12 h and a maximum peak hardness value of 71 HV after 21 h. The hardness of the pre-deformed sample decreased slowly at first and decreased significantly after 24 h. The hardness of the pre-deformed sample is enhanced to a value of 71.1 HV after 21 h. Thus, seen in Fig. 3, the peak-aged state was obtained when aging for 21 h.

3.2 Microstructure and Texture

Figure 4 presents the three-dimensional inverse pole figure maps and pole figures of the STA and PDA samples. STA has a fully recrystallized structure and a typical basal texture with two peaks of the (0002) poles that are slightly inclined from the ND towards TD, as shown in Fig. 4b. The prismatic planes were randomly distributed. After cross compression, a large number of twin lamellae are generated in the PDA sample which shows three texture components with the (0002) poles close to the ND, TD, and RD, respectively. The types of twins are analyzed and shown in Fig. 5. The (0002) poles of the red regions are close to the ND and similar

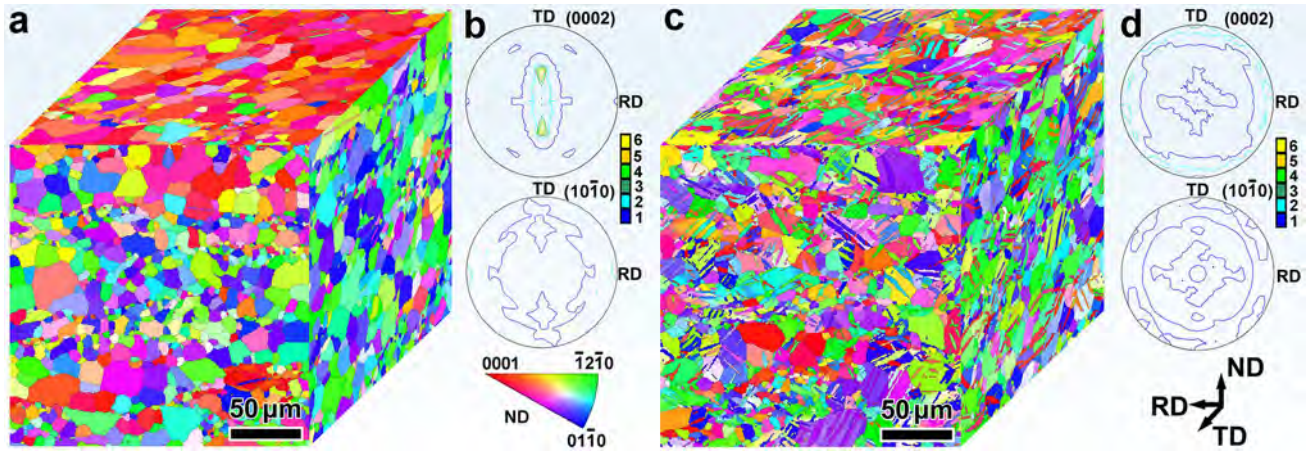

Fig. 4 Three-dimensional inverse pole figure maps and pole figures by XRD: **a**, **b** STA, **c**, **d** PDA

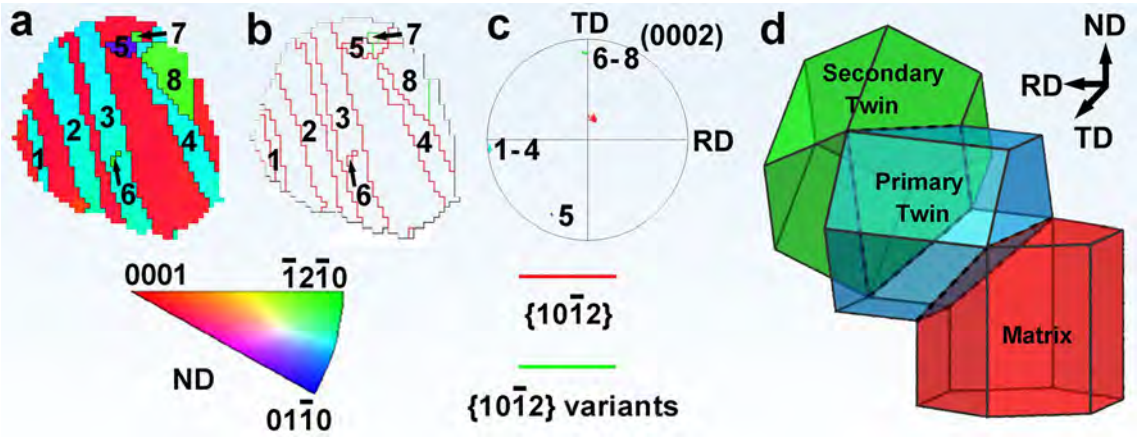

Fig. 5 **a** Inverse pole figure map, **b** boundary misorientation map, **c** (0002) pole figure of a selected grain in the PDA sample; **d** schematic diagram of the $\{10\bar{1}2\}$–$\{10\bar{1}2\}$ secondary twin

to the orientation of most grains in the original materials, and therefore, they constitute the matrix. Twins 1–5 show boundaries with a misorientation angle of 86° and spin axis of $<1\bar{2}10>$ with respect to the matrix signifying the typical $\{10\bar{1}2\}$ twin boundary. That is, they are the primary $\{10\bar{1}2\}$ twins. Generally, there are six variants of the $\{10\bar{1}2\}$ twins. The basal pole of twin 5 is different from those of twin 1–4 and Twin 5 is thus the different variant from twins 1 to 4. Since twins 6–8 also have a $\{10\bar{1}2\}$ twin boundary with the primary twins, they are the $\{10\bar{1}2\}$–$\{10\bar{1}2\}$ secondary twins. Figure 5d shows the orientation relationship of the $\{10\bar{1}2\}$–$\{10\bar{1}2\}$ secondary twin, and obviously, the $\{10\bar{1}2\}$–$\{10\bar{1}2\}$ secondary twinning rotates the basal plane poles to the TD. A dual twin structure with the $\{10\bar{1}2\}$ primary twin and $\{10\bar{1}2\}$–$\{10\bar{1}2\}$ secondary twins exists in the PDA sample. The $\{10\bar{1}2\}$ primary twin accounts for approximately 24% and $\{10\bar{1}2\}$–$\{10\bar{1}2\}$ twins account for 1.7%.

Figure 6a and b presents the distribution and morphology of the precipitates in the STA and PDA samples under the peak-aged condition. The precipitates in the ZK60 alloy consist of mainly the β′ (Mg_4Zn_7 or Mg_2Zn_3) phase and β″ ($MgZn_2$) phase [40]. The rod-like β′ phase is perpendicular to the (0001) basal plane and the orientation relationship is $[0001]_{\beta'}//[11\bar{2}0]_{\alpha}$ and $(11\bar{2}0)_{\beta'}//(0001)_{\alpha}$ between β′ and α-Mg. The disk-shape β″ phase is parallel to the (0001) basal plane and the orientation relationship is $[11\bar{2}0]_{\beta''}//[10\bar{1}0]_{\alpha}$ and $(0001)_{\beta''}//(0001)_{\alpha}$ between β″ and α-Mg [41]. Similar precipitate morphology is revealed in Fig. 6. The rod-like β′ phases (marked as "1" in Fig. 6a) and disk-shape β″ phases (marked "2" in Fig. 6) are the major precipitates in the STA sample. In the PDA sample, the rod-like β′ phases (marked as "1" in Fig. 6b) decrease dramatically, while a large number of disk-shape β″ phases (marked as "2" in Fig. 6b) can be observed from both the twins and matrix. In addition, many

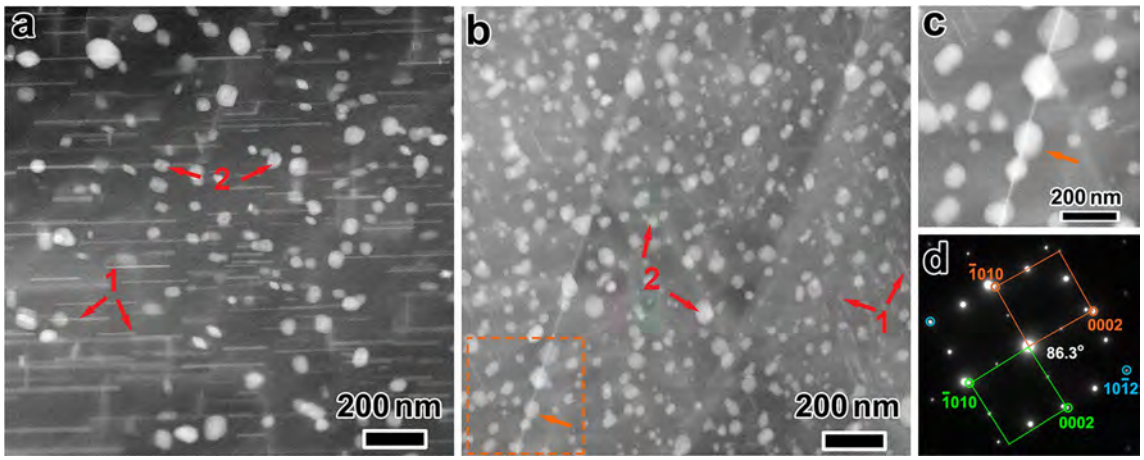

Fig. 6 STEM images showing the distribution and morphology of the precipitates: **a** STA sample, **b** PDA sample; **c** high-magnification view of the selected region denoted by the orange rectangles in **b**; **d** indexing of the selected-area diffraction pattern of the deformation twin in **c**

Table 1 Mechanical properties of the STA samples and PDA samples (CYS and TYS are the compression yield strength and tension yield strength, respectively)

		Yield strength (MPa)	Ultimate strength (MPa)	Elongation (%)	CYS/TYS or TYS/CYS
ND direction	STA sample-T	114	363	25.9	0.81
	STA sample-C	141	303	13.6	
	PDA sample-T	150	362	27.7	0.99
	PDA sample-C	149	323	15.1	
RD direction	STA sample-T	206	339	22.2	0.62
	STA sample-C	127	352	12.6	
	PDA sample-T	183	353	23.0	0.98
	PDA sample-C	179	383	13.7	
TD direction	STA sample-T	143	340	26.8	0.83
	STA sample-C	119	324	15.1	
	PDA sample-T	162	364	32.9	0.99
	PDA sample-C	164	345	16.8	

precipitates appear from the twin boundaries. The density of the fine disk-shape β″ phases in the PDA sample is larger than that in the STA sample. The results demonstrate that the existence of twins is the result of an increase in the disk-shape β″ phases. Figure 6a and b shows that the density of the finer disk-shape β″ phases in the PDA samples is larger than that in the STA samples on account of the twin boundary created by pre-deformation.

3.3 Mechanical Properties

The stress–strain curves of the STA and PDA samples under both tension and compression along the ND, RD, and TD are displayed in Fig. 7. Under compression along the TD and RD and tension along the ND, the plots of the STA samples have a sigmoidal shape known to be the typical feature of $\{10\bar{1}2\}$ twinning dominated deformation [[20]]. With regard to the PDA samples, the sigmoidal shape can also be observed from the curves under compression along the ND, RD, and TD.

The mechanical properties derived from the curves are listed in Table 1. All the compressive yield strengths of the PDA samples are higher than those of the STA samples along the same direction. The tension yield strengths of the PDA samples are also much higher than those of the STA samples besides along the RD. The ultimate strength of the PDA samples increases under both tension and compression besides tension along the TD. Compared to the STA samples, elongation of the PDA samples does not decrease. The ratio of the compression yield strength to tension yield strength is used to evaluate the tension–compression yield asymmetry. A ratio closer to 1 means a weaker tension–compression yield asymmetry. The STA samples have a tension–compression yield asymmetry with 0.81 for ND, 0.83 for TD, and 0.62 for RD, respectively. However, it is found that the yield asymmetry is improved evidently in PDA samples. The

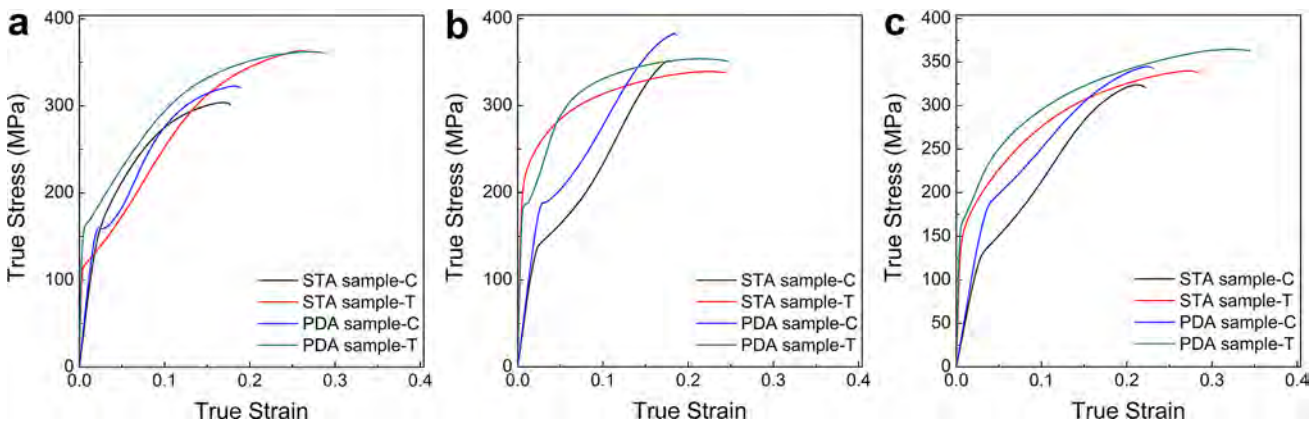

Fig. 7 Stress–strain curves under tension and compression: **a** ND, **b** RD, **c** TD (C and T represent compression and tension, respectively)

ratios of the PDA samples are close to 1 with 0.99 for ND, 0.99 for TD, and 0.98 for RD, respectively. Obviously, the tension–compression yield asymmetry was removed completely by the dual twin structure; furthermore, the strength was increased without undermining the ductility.

3.4 Corrosion Behavior

3.4.1 Corrosion Rates

The amount of emitted hydrogen in Hank's solution is monitored as a function of immersion time to evaluate the corrosion rate as shown in Fig. 8. For the STA samples, the plane RD-TD yields the largest hydrogen volume, whereas the smallest is observed from the plane ND-TD. After immersion for 76 h, the volume of hydrogen from the STA plane RD-TD is approximately 1.6 times that from the STA plane ND-TD thus revealing a strong corrosion anisotropy. Similarly, for the PDA samples, the plane RD-TD shows the highest corrosion rate and that of the plane ND-TD is the smallest. Compared to the STA samples, the corrosion rate of the plane RD-TD of PDA samples drops slightly and those of the plane ND-TD and surface plane ND-RD increase slightly. After immersion for 76 h, the corrosion rate of the PDA plane RD-TD is approximately 1.2 times of that of the PDA plane ND-TD suggesting that the dual twin structure reduces the corrosion anisotropy without increasing the corrosion rate significantly.

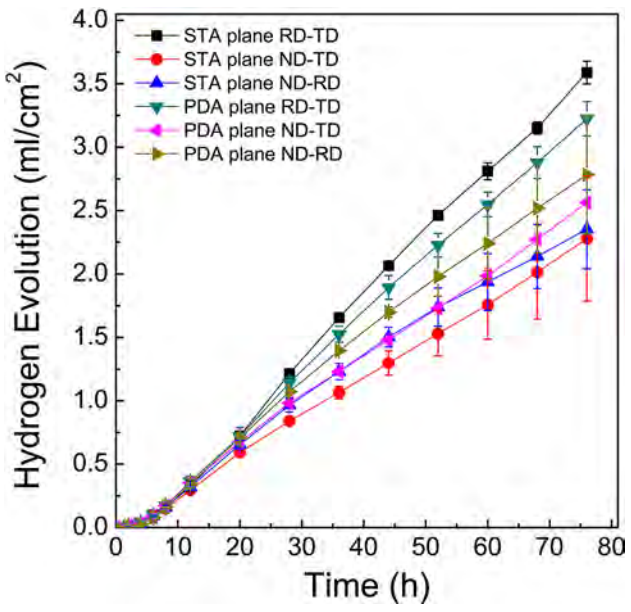

Fig. 8 Hydrogen evolution as a function of immersion time in Hank's solution

3.4.2 Corrosion Morphology

The corrosion morphology of the STA and PDA samples after immersion in Hank's solution for 6, 24, and 72 h is depicted in Figs. 9, 10 and 11. No pitting corrosion is observed from the STA samples and PDA samples after 6 h. Many cracks appear as shown in Fig. 9e and l, Fig. 10e and l, and Fig. 11e and l due to water loss from the corrosion products during electron beam bombardment [42]. As shown in Fig. 9d and k, Fig. 10d and k, as well as Fig. 11d and k, the surface is covered partially by protective corrosion products. After 24 h, corrosion pits are observed from all the STA and PDA samples (Fig. 9b and i, Fig. 10b and i, as well as Fig. 11b and i). After 72 h, many large and deep pits emerge. All in all, the corrosion morphology varies only slightly between the STA and PDA samples as well as among the plane RD-TD, plane ND-TD, and plane ND-RD.

3.4.3 Electrochemical Corrosion Behavior

Figure 12 shows the OCP of the STA and PDA samples during immersion in Hank's solution for 72 h and the OCP curves exhibit a similar tendency. The OCP rises initially in the beginning 12 h and stabilizes at approximately -1.51 V vs. SCE despite some fluctuations. Figure 13 presents the potentiodynamic polarization curves of the STA and PDA samples in Hank's solution. Branches from both the anodic dissolution reaction and cathodic reaction are observed to avoid the effects of surface modification [43]. The measured cathodic and anodic curves exhibit no significant variations between the STA and PDA samples as well as among plane RD-TD, plane ND-TD, and plane ND-RD. The corrosion potentials (E_{corr} referenced to the saturated calomel electrode SCE) and corrosion current densities (i_{corr}) obtained from the potentiodynamic polarization curves are listed in Table 2. E_{corr} varies within −1.605 to −1.568 V vs. SCE and i_{corr} within 18.08–26.75 μA/cm^2. Similarly, there is only a small difference for both E_{corr} and i_{corr} among the samples.

Owing to the nondestructive nature and continuous monitoring, EIS is a powerful tool to analyze the sub-processes [44]. The Nyquist spectra of the STA and PDA samples are acquired from the Hank's solution after immersion for different time as shown in Fig. 14. For an immersion time of 5 min, two time constants are observed as revealed by a high-frequency capacitance loop and the other low-frequency capacitance loop. However, the samples after exposure for 24 and 72 h exhibit one high-frequency capacitive and one low-frequency inductive loop. When the low-frequency inductance loop appears, the difference of frequency values is small in Fig. 14b and c. The high-frequency capacitance loop is attributed to charge transfer and film effects [[7]], and the diameter is estimated to be equal to the charge

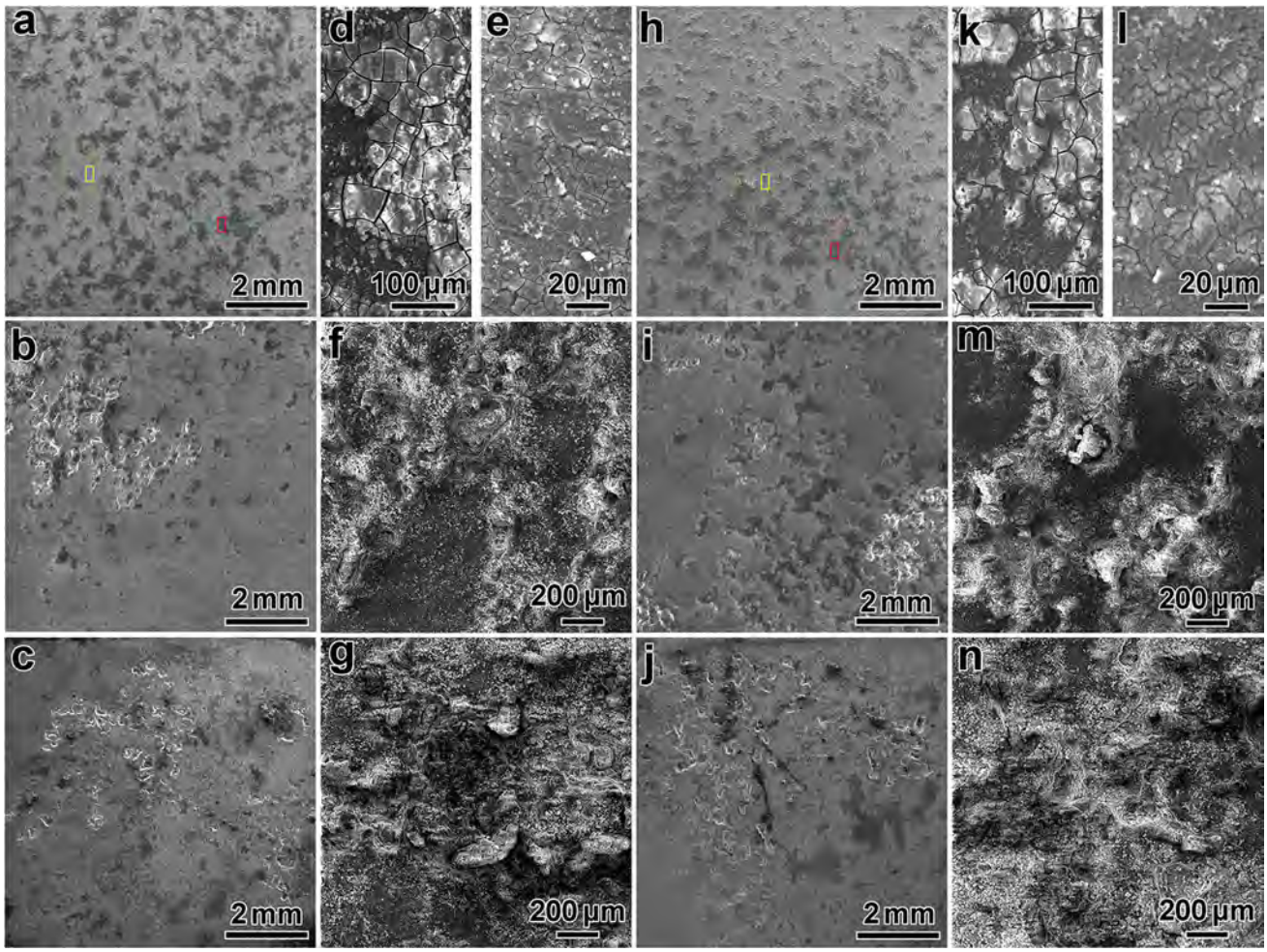

Fig. 9 SEM micrographs of the plane RD-TD of the STA samples after immersion in Hank's solution for: **a**, **d, e** 6 h, **b**, **f** 24 h, **c**, **g** 72 h; PDA sample for **h**, **k**, **l** 6 h, **i**, **m** 24 h, **j**, **n** 72 h. **d**, **e** are the high-magnification views of the selected regions shown by the red rectangle and yellow rectangle in **a**, **k, l** are the high-magnification images of the selected regions denoted by the red rectangle and yellow rectangle in **h**

transfer resistance in the electrochemical reaction [45]. The low-frequency capacitance loop arises from mass transport relaxation in the solid phase [46]. With regard to the low-frequency inductive loop, it is associated with dissolution of the partially protective film [47] or chemical reaction between absorbed Mg^{2+} and H_2O [48].

Fitting of the electrochemical impedance response is shown in Fig. 14. Owing to the inductive behavior after immersion for 24 h (Fig. 14b) and 72 h (Fig. 14c) and its absence after 5 min (Fig. 14a), the model in Fig. 15a is employed to fit the data in Fig. 14a and that in Fig. 15b is used to fit data in Fig. 14b and Fig. 14c. The fitted EIS results of the STA and PDA samples after different immersion time are listed in Tables 3, 4 and 5. R_s represents the solution resistance between the working electrode and reference electrode. R_t shows the charge-transfer resistance and Q_{dl} is the capacitance to describe the electrical double layer at the interface. R_t and Q_{dl} describe the first high-frequency capacitance loop and Q_{dl} is the constant-phase element associated with the non-ideal capacitance to verify the inhomogeneous surface reactions determined by Y_{dl} and n_{dl}. A larger R_t signifies a better corrosion resistance due to the smaller dissolution rate of the Mg matrix [49], whereas a smaller Y_{dl} indicates that the surface film is compact. R_t of the STA plane RD-TD is the smallest for the different immersion time. The results are consistent with the data obtained by hydrogen evolution. R_f and Q_f are the film resistance and capacity and describe the second low-frequency capacitance loop. Q_f is the constant-phase element representing the corrosion product layer on the surface [50], and R_L and L stand for the resistance and inductance, respectively, and describe the inductance loop arising from initiation of localized corrosion at low frequencies[51]. The induction loops of the STA and PDA samples after immersion for 24 and 72 h demonstrate the occurrence of corrosion. With regard to the STA samples and PDA samples after immersion for 5 min, the absence of induction loops may stem from corrosion attack during the

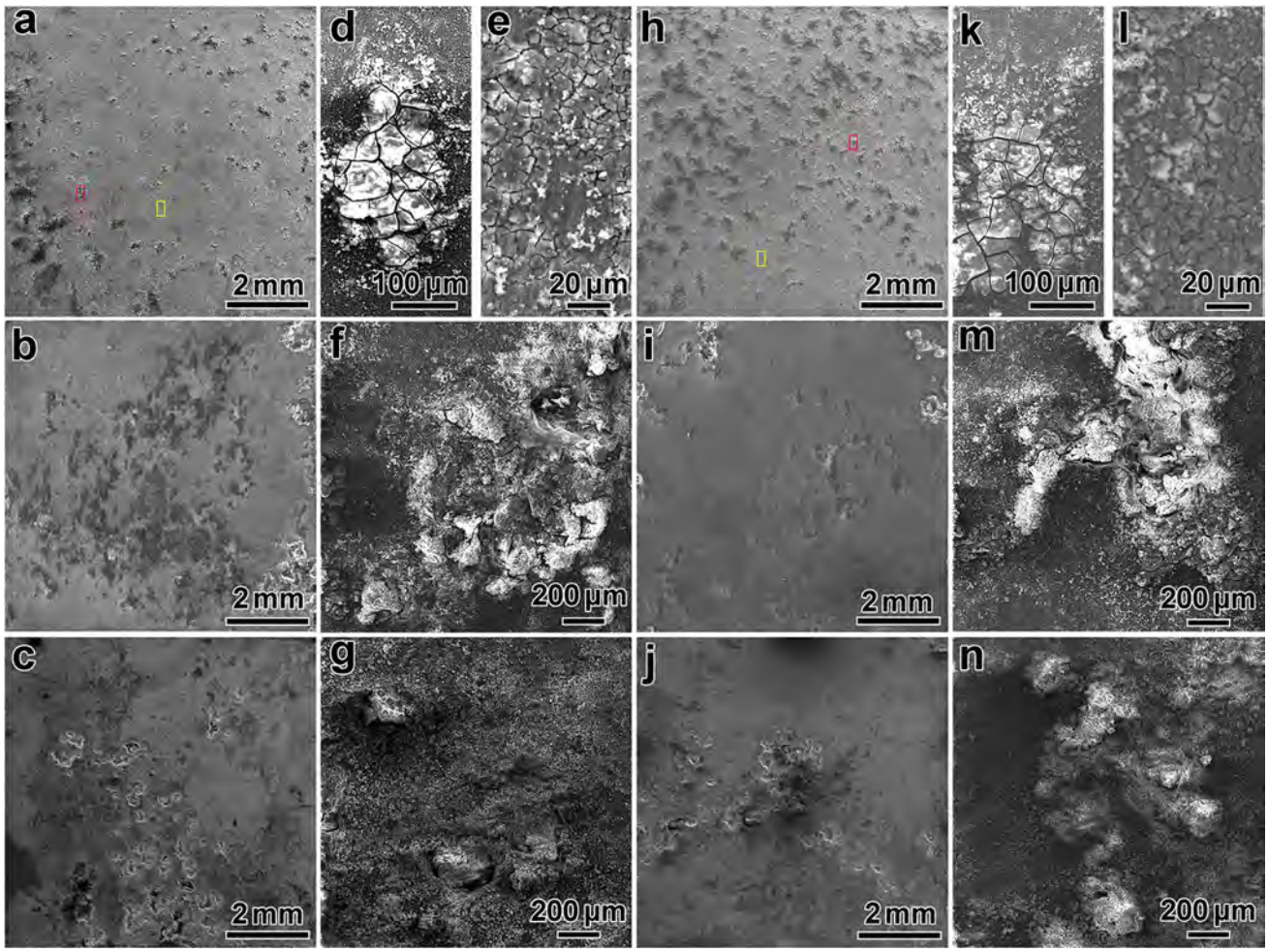

Fig.10 SEM micrographs of the plane ND-TD of the STA samples after immersion in Hank's solution for: **a**, **d**, **e** 6 h, **b** and **f** 24 h, and **c** and **g** 72 h; PDA samples for **h**, **k** and **l** 6 h, **i**, **m** 24 h, **j** and **n** 72 h. **d**, **e** are the high-magnification images of the selected regions shown by the red rectangle and yellow rectangle in **a**, **k** and **l** are the high-magnification views of the selected regions denoted by the red rectangle and yellow rectangle in **h**

short immersion time. In general, the fitted EIS spectra agree with the results obtained by hydrogen evolution.

4 Discussion

4.1 Effects of Twins on the Tension–Compression Yield Asymmetry

At room temperature, $\{10\bar{1}2\}$ twinning in the Mg alloy has a low CRSS and is activated by compressive stress perpendicular to the *c*-axis or tensile stress parallel to the *c*-axis. Therefore, for the Mg alloy with the (0002) poles largely parallel to the ND, compression along the TD or RD often leads to the predominant $\{10\bar{1}2\}$ twinning deformation [25]. Under compression, $\{10\bar{1}2\}$ twinning rotates the basal poles by approximately 86° towards the compression axis. Hence, pre-compression along the RD generates primary $\{10\bar{1}2\}$ twins with the (0002) poles close to the RD. Under recompression along the TD, both the orientations of the untwined matrix and primary $\{10\bar{1}2\}$ twins are favorable to $\{10\bar{1}2\}$ twinning. That is, $\{10\bar{1}2\}$ twinning occurs in both the untwined matrix and $\{10\bar{1}2\}$ primary twins under recompression along the TD forming $\{10\bar{1}2\}$ primary twins in the matrix and $\{10\bar{1}2\}$–$\{10\bar{1}2\}$ secondary twins in the primary twins. The (0002) poles of the new twins are close to the TD and so in the PDA samples, there are four types of microstructures, the untwined matrix, $\{10\bar{1}2\}$ primary twins with the (0002) poles close to the RD, $\{10\bar{1}2\}$ primary twins with the (0002) poles close to the TD, as well as $\{10\bar{1}2\}$–$\{10\bar{1}2\}$ secondary twins with the (0002) poles close to the TD. The discussion is confirmed by the results in Fig. 5.

Compression along the TD/RD of the basal-textured Mg alloy plate constitutes the predominant $\{10\bar{1}2\}$ twinning

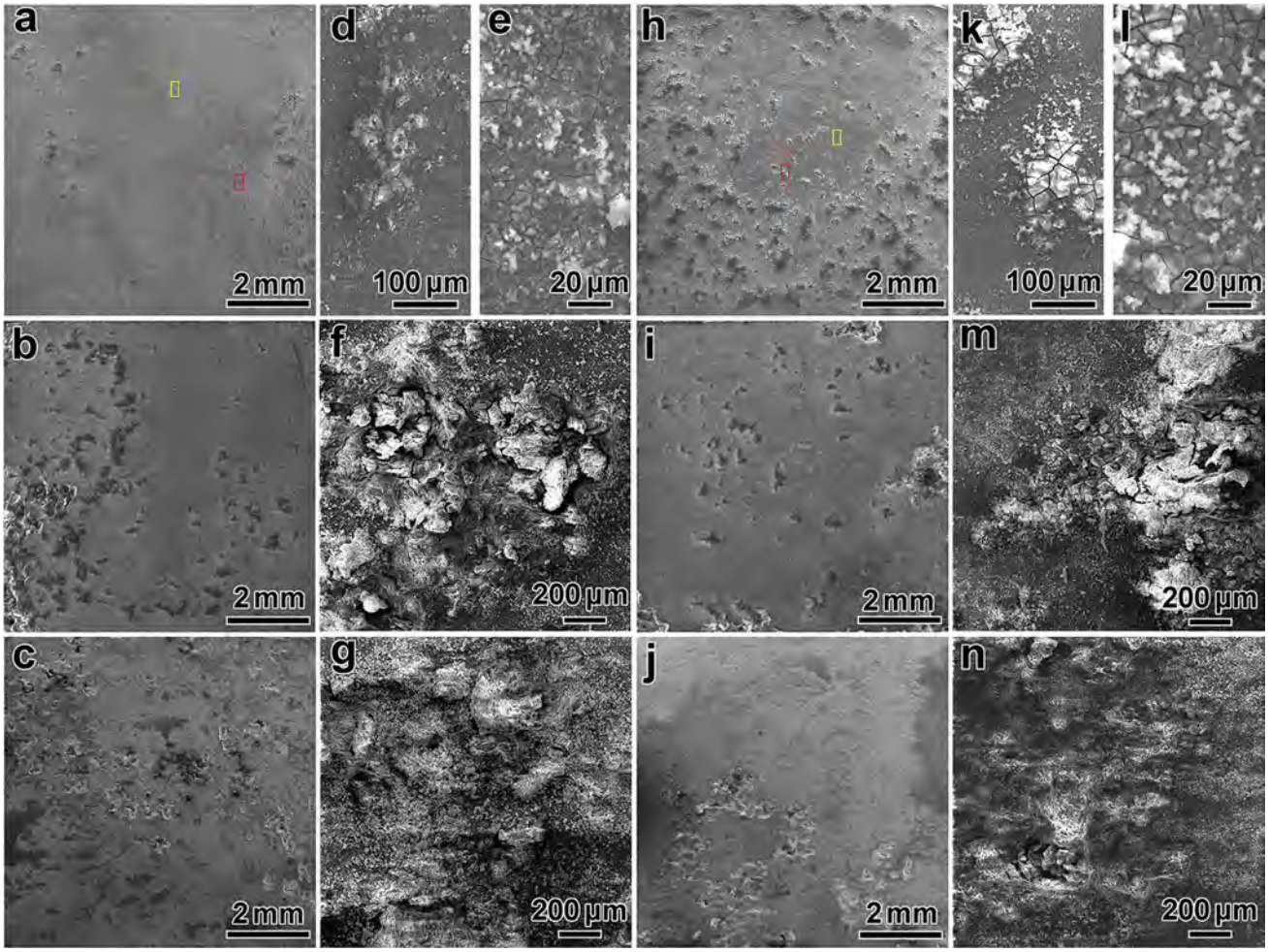

Fig. 11 SEM micrographs of the plane ND-RD of the STA samples after exposure to Hank's solution for: **a**, **d**, **e** 6 h, **b**, **f** 24 h, **c**, **g** 72 h; PDA samples for **h**, **k**, **l** 6 h, **i**, **m** 24 h, **j**, **n** 72 h. **d**, **e** are the high-magnification images of the selected regions shown by the red rectangle and yellow rectangle in **a**, **k**, **l** are the high-magnification views of the selected regions denoted by the red rectangle and yellow rectangle in **h**

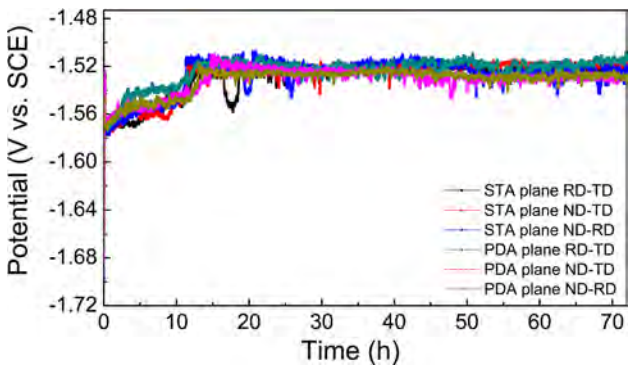

Fig. 12 OCP variations as a function of immersion time in Hank's solution up to 72 h

deformation, while tension along the TD/RD is a prismatic slip predominant one. Tension along the ND is often a $\{10\bar{1}2\}$ twinning predominant deformation [52] and compression along the ND is a basal slip predominant one [53]. It is well known that the CRSS for prismatic slip is 3–5 times that for $\{10\bar{1}2\}$ twinning [54] thereby resulting in lower yield strength of compression along the TD/RD compared to the tensile yield strength along the RD/TD as confirmed by the results in Table 1. Although the CRSS of basal slip is close to that of $\{10\bar{1}2\}$ twinning, compression along the ND often has a smaller Schmid factor which leads to a lower tension yield strength along the ND than that of compression along the ND [55]. Hence, the reasons for the strong tension–compression yield asymmetry are: (1) microscopic yield during tension and the compression dominated by the single but different deformation modes (either slips or $\{10\bar{1}2\}$ twinning) and (2) lower CRSS for $\{10\bar{1}2\}$ twinning than that for slips.

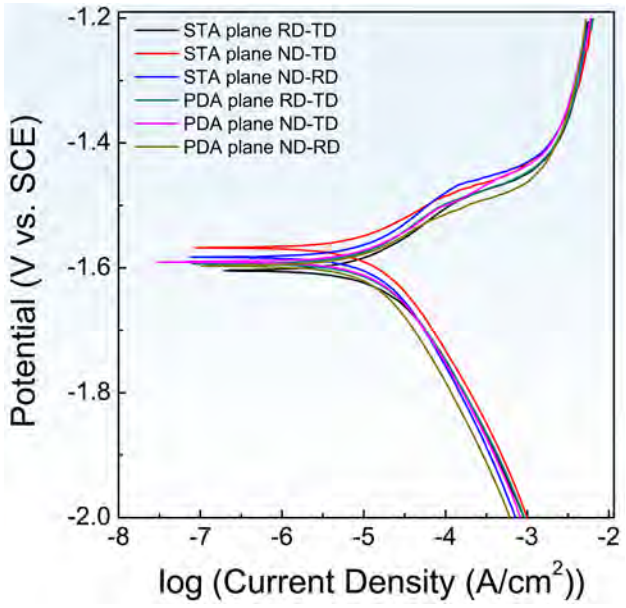

Fig. 13 Potentiodynamic polarization curves of the STA and PDA samples in Hank's solution

Table 2 E_{corr} and i_{corr} derived from the potentiodynamic polarization curves

	E_{corr} (V vs. SCE)	i_{corr} (μA cm^{-2})
STA plane RD-TD	−1.605	26.75
STA plane ND-TD	−1.568	18.84
STA plane ND-RD	−1.583	19.27
PDA plane RD-TD	−1.594	21.46
PDA plane ND-TD	−1.591	20.53
PDA plane ND-RD	−1.597	18.08

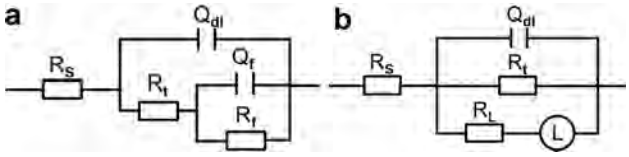

Fig. 15 EIS models of the STA and PDA samples after immersion in Hank's solution: **a** 5 min, **b** 24 h and 72 h

The PDA samples are composed of an untwined matrix, $\{10\bar{1}2\}$ primary twins with the (0002) poles toward to the RD (named as primary twin 1), $\{10\bar{1}2\}$ primary twins with the (0002) poles toward the TD (named as primary twin 2), and $\{10\bar{1}2\}$–$\{10\bar{1}2\}$ secondary twins with the (0002) poles close to the TD (named as secondary twin). The deformation mechanism of twins is related to both the type and orientation of twins as well as loading paths. The theoretical analysis of the deformation mode of twins in the PDA samples is listed in Table 6. To corroborate the analysis, quasi in situ EBSD is performed on the PDA samples under compression along the RD and ND as shown in Figs. 16 and 17, respectively. In quasi in situ EBSD mapping, the sample is measured first, reloaded outside the SEM, and then re-measured at the same region.

As shown in Fig. 16, after compression, a large portion of the residual untwined matrix is transformed into the $\{10\bar{1}2\}$ primary twins (area of the $\{10\bar{1}2\}$ twin increasing from 27.6% in Fig. 16a to 54% in Fig. 16b). Figure 16c and d depicts the micrographs of the selected grains before and after compression (denoted by the black rectangles in Fig. 16a and b). Regions 3 ($\{10\bar{1}2\}$ primary twin) and 2 ($\{10\bar{1}2\}$ twin variants) swallow the red regions 1 (the matrix, Fig. 16c) after compression in the typical twin growth process and region 4 ($\{10\bar{1}2\}$–$\{10\bar{1}2\}$ secondary twin) remains. Figure 16d shows the $\{10\bar{1}2\}$–$\{10\bar{1}2\}$

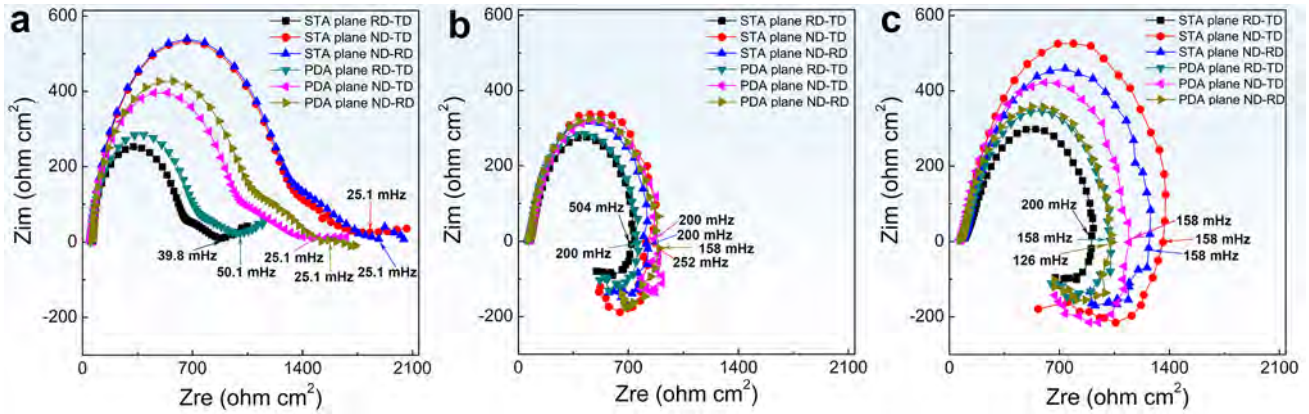

Fig. 14 Nyquist plots of the STA and PDA samples after immersion in Hank's solution: **a** 5 min, **b** 24 h, **c** 72 h

secondary twin (region 6) and $\{10\bar{1}2\}$–$\{10\bar{1}2\}$ secondary twin variants (region 7 and region 8) disappear and it corresponds to detwinning from the $\{10\bar{1}2\}$–$\{10\bar{1}2\}$ secondary twin to the $\{10\bar{1}2\}$ primary twin. Some matrix (region 1) also disappears due to the growth of the $\{10\bar{1}2\}$ primary twin (region 2). Some new $\{10\bar{1}2\}$ twins in the $\{10\bar{1}2\}$ primary twins are observed (for example, the twin denoted by the black arrow in Fig. 16b) corresponding to the $\{10\bar{1}2\}$–$\{10\bar{1}2\}$ secondary twins. That is, growth of $\{10\bar{1}2\}$ twins, detwinning of the $\{10\bar{1}2\}$–$\{10\bar{1}2\}$ secondary twins, and $\{10\bar{1}2\}$ secondary twinning in the primary twins occur under re-compression along the RD of the PDA samples. Under the tension along RD, the $\{10\bar{1}2\}$ primary twins and the $\{10\bar{1}2\}$–$\{10\bar{1}2\}$ secondary twins are both beneficial to the prismatic slip. However, some the $\{10\bar{1}2\}$ primary twins with (0002) poles near RD are prone to detwin. Under the compression along TD, in general the $\{10\bar{1}2\}$ twins appear in both the $\{10\bar{1}2\}$ primary twins and the untwined matrix. Under the tension along TD, the $\{10\bar{1}2\}$ primary twins are favorable for prismatic slip, but the $\{10\bar{1}2\}$ primary twins with (0002) poles toward RD and the $\{10\bar{1}2\}$–$\{10\bar{1}2\}$ secondary twins tend to detwin.

After compression of 3% along the ND (Fig. 17), many $\{10\bar{1}2\}$ twins are converted into the matrix (area of the $\{10\bar{1}2\}$ twin resulting in the decrease from 30.5% in Fig. 17a to 15.9% in Fig. 17b). Figure 17c and d shows the microstructure evolution of the selected grains (denoted by the black rectangles in Fig. 17a and b). The $\{10\bar{1}2\}$ primary twins (region 2), $\{10\bar{1}2\}$ primary twin (region 2), and $\{10\bar{1}2\}$–$\{10\bar{1}2\}$ secondary twins (region 3) in Fig. 17c narrow or disappear after compression corresponding to detwinning of the $\{10\bar{1}2\}$ twin. Meanwhile, tertiary twins (regions 5 and 6) are generated from the $\{10\bar{1}2\}$–$\{10\bar{1}2\}$ secondary twins (region 3). As shown in Fig. 17d, the $\{10\bar{1}2\}$ primary twins (region 2) and $\{10\bar{1}2\}$ primary twin variants (region 3) before compression turn into the matrix after compression. However, most of the $\{10\bar{1}2\}$–$\{10\bar{1}2\}$ secondary twins (regions 4 and 5) are preserved after compression. Under the tension along ND, the $\{10\bar{1}2\}$ primary twins frequently occur in the untwined matrix; meanwhile, the orientation of

Table 3 Fitted EIS results using EC in Fig. 15a for the STA and PDA samples after immersion for 5 min

Sample	R_s (Ω cm^2)	Y_{dl} ($\mu\Omega^{-1}$ cm^{-2} s^{-n})	n_{dl}	R_t (Ω cm^2)	Y_f ($\mu\Omega^{-1}$ cm^{-2} s^{-n})	n_f	R_f (Ω cm^2)
STA plane RD-TD	54.15	16.86	0.9292	574.8	3423	0.6748	316.6
STA plane ND-TD	66.42	11.34	0.9344	1206	1742	0.6661	561
STA plane ND-RD	58.88	11.82	0.9235	1241	1668	0.7417	553.6
PDA plane RD-TD	52.78	16.49	0.9279	652.5	2673	0.6696	372.2
PDA plane ND-TD	54.85	14.16	0.9292	916.2	2091	0.7298	499
PDA plane ND-RD	57.44	13.7	0.9203	994.1	1817	0.7212	492.2

Table 4 Fitted EIS results using EC in Fig. 15b for the STA and PDA samples after immersion for 24 h

Sample	R_s (Ω cm^2)	Y_{dl} ($\mu\Omega^{-1}$ cm^{-2} s^{-n})	n_{dl}	R_t (Ω cm^2)	L (H cm^{-2})	R_L (Ω cm^2)
STA plane RD-TD	76.14	127.3	0.8165	698.2	5991	1317
STA plane ND-TD	77.74	125.8	0.8633	812.6	6811	809.7
STA plane ND-RD	66.19	133.3	0.8398	805.8	8584	1245
PDA plane RD-TD	67.33	116.6	0.8496	719	6505	1104
PDA plane ND-TD	68.54	154.8	0.7859	898	12,220	2010
PDA plane ND-RD	66.04	137	0.8368	856.6	8264	1240

Table 5 Fitted EIS results using EC in Fig. 15b for the STA and PDA samples after immersion for 72 h

Sample	R_s (Ω cm^2)	Y_{dl} ($\mu\Omega^{-1}$ cm^{-2} s^{-n})	n_{dl}	R_t (Ω cm^2)	L (H cm^{-2})	R_L (Ω cm^2)
STA plane RD-TD	94.2	143.8	0.6636	944.3	5816	1691
STA plane ND-TD	82.62	108.8	0.7698	1423	8255	1572
STA plane ND-RD	83.71	124.9	0.702	1397	7661	2236
PDA plane RD-TD	81.4	102.4	0.724	1017	8425	1515
PDA plane ND-TD	70.4	117.1	0.7808	1149	9071	1265
PDA plane ND-RD	70.1	132.7	0.7402	1043	8800	1500

Table 6 Deformation modes of different types of twins under compression or tension along the ND, RD, and TD

	Type of twin	Deformation mode
Compression // ND	Primary twin 1	Detwinning
	Primary twin 2	Detwinning
	Secondary twin	Tertiary twinning
Tension // ND	Primary twin 1	$\{10\bar{1}2\}$ twin growth
	Primary twin 2	$\{10\bar{1}2\}$ twin growth
	Secondary twin	Prismatic slip
Compression // RD	Primary twin 1	$\{10\bar{1}2\}$ twin growth
	Primary twin 2	$\{10\bar{1}2\}$–$\{10\bar{1}2\}$ secondary twinning
	Secondary twin	Detwinning
Tension // RD	Primary twin 1	Detwinning
	Primary twin 2	Prismatic slip
	Secondary twin	Prismatic slip
Compression // TD	Primary twin 1	$\{10\bar{1}2\}$–$\{10\bar{1}2\}$ secondary twinning
	Primary twin 2	$\{10\bar{1}2\}$ twin growth
	Secondary twin	$\{10\bar{1}2\}$–$\{10\bar{1}2\}$ twin growth
Tension // TD	Primary twin 1	Prismatic slip
	Primary twin 2	Detwinning
	Secondary twin	Detwinning

the $\{10\bar{1}2\}$ primary twins and the $\{10\bar{1}2\}$–$\{10\bar{1}2\}$ secondary twins are conducive to the prismatic slip. Under the compression along RD, the $\{10\bar{1}2\}$ primary twins with (0002) poles near RD prefer to grow up in the untwined matrix. The $\{10\bar{1}2\}$–$\{10\bar{1}2\}$ secondary twins with (0002) poles close to TD tend to detwin in the $\{10\bar{1}2\}$ primary twins. All above discussion show that two or three deformation modes, e.g., the slips, the $\{10\bar{1}2\}$ twinning and the detwinning, can be initiated simultaneously during the tension and compression, which is an important reason for reducing tension–compression yield asymmetry in the PDA samples. Hence, both detwinning of the $\{10\bar{1}2\}$ primary twins and $\{10\bar{1}2\}$ twinning in the $\{10\bar{1}2\}$–$\{10\bar{1}2\}$ twins appear under compression along the ND of the PDA samples and the experimental results are in line with the analysis listed in Table 6.

Table 6 shows that the microstructure of the PDA samples favors two or three deformation modes under tension or compression along the same direction, i.e., detwinning and $\{10\bar{1}2\}$ twinning for compression along the ND or twin growth and prismatic slip for tension along the ND. Detwinning and twin growth are twin boundary migration processes with lower activation stress than twinning nucleation [56]. Wu et al. [57] have reported that the activation stress of detwinning is only half that of twinning. Although $\{10\bar{1}2\}$ twinning has a lower CRSS than prismatic slip, grain refinement is more effective in hardening twinning. According to Yu et al. [58], the $\{10\bar{1}2\}$ twin boundaries are effective barriers against twinning and poor barriers against slip, thus rendering the twin boundary more effective in hardening twinning than slips compared to grain boundaries. For example, the yield strength of the $\{10\bar{1}2\}$ twinning predominant deformation (126 MPa) is similar to that of the prismatic slip predominant one (127 MPa) [58]. The activation stress for twinning nucleation here is expected to be close to that of prismatic slip [58], and therefore, both $\{10\bar{1}2\}$ twinning and prismatic slip are hard deformation modes in the pre-twinned

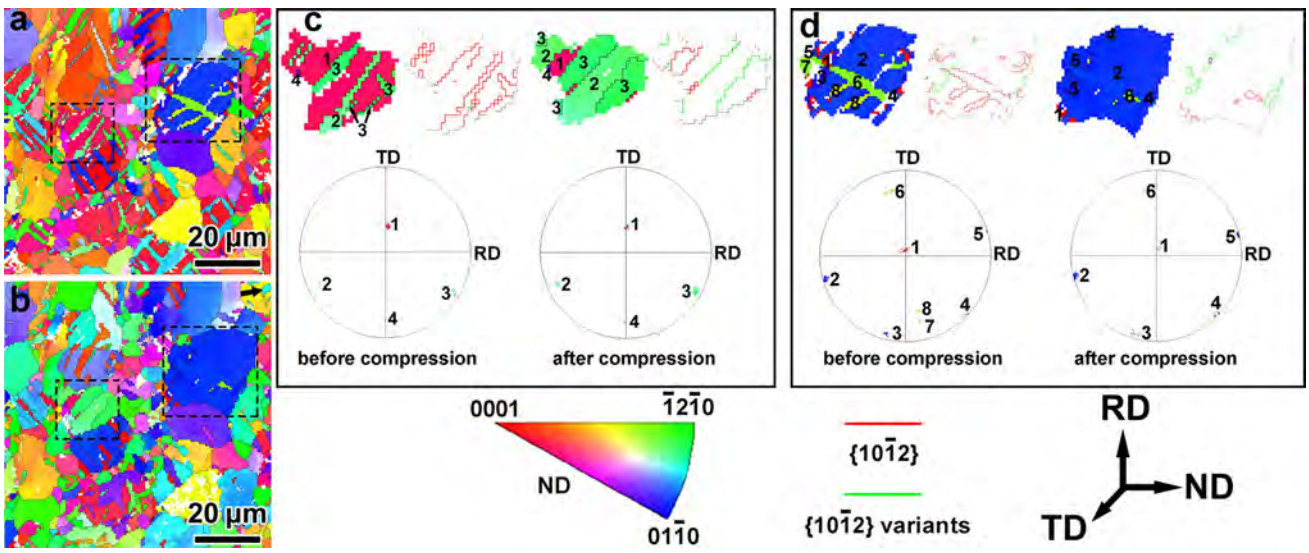

Fig. 16 Microstructure and crystallographic orientation evolution **a** before and **b** after 3% compression along the RD of the PDA samples, **c**, **d** crystallographic orientations of the selected grains in **a**, **b**

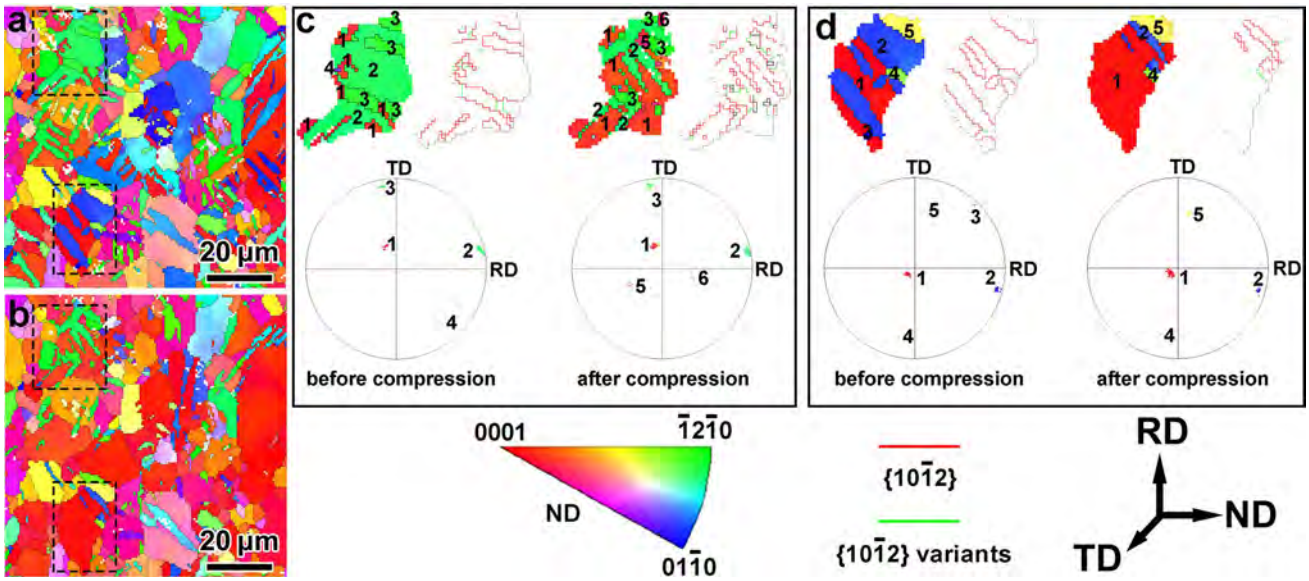

Fig. 17 Microstructure and crystallographic orientation evolution **a** before and **b** after 3% compression along the ND of the PDA samples, **c**, **d** crystallographic orientations of the selected grains in **a**, **b**

Mg alloy, whereas those for twin growth and detwinning are easy deformation modes. There are thus different deformation modes including both hard and easy ones under tension and compression and this contributes to the lower tension–compression yield asymmetry in the PDA samples.

Previous investigations have shown that grain refinement by twin lamellae can improve the CRSS for twinning and slip, which will enhance yield strength [59]. A CYS/TYS of 0.4–0.5 often exists in coarse-grained Mg alloys, while increases to 0.9 with refining grain size to 1.9 μm via twin lamellas [25]. In this work, the hybrid twin structure can greatly refine grain size from 10.9 to 5.7 μm. In addition, the existence of precipitates also can also hinder the propagation of the {$10\bar{1}2$} twinning resulting in a lower yield asymmetry [40]. Therefore, the activation stresses for all types of {$10\bar{1}2$} twinning in PDA samples should be higher than that of {$10\bar{1}2$} twinning in STA samples without pre-deformation. Similarly, the CRSSs for the basal slips and the prismatic slips in the PDA samples are also higher than that in the STA samples. For ZK60 alloy, the yield asymmetry is improved by the presence of disk-like precipitates while becomes worse by the appearance of rod-like precipitates, but the predominant deformation mode does not change after precipitation [60]. In Fig. 6, the rod-like β′ phases and disk-shape β″ phases are the major precipitates in the STA sample. However, in the PDA sample, the rod-like β′ phases decrease dramatically, while a large number of disk-shape β″ phases can be observed from both the twins and matrix. Therefore, the presence of precipitates disk-shape β″ phases improve the tension–compression yield asymmetry in the PDA samples, but do not change the dominated deformation mode [60].

4.2 Effects of Twins on Corrosion Anisotropy

A strong basal texture forms easily after thermomechanical processing of Mg alloys and often generates a strong corrosion anisotropy. For example, the cross-sectional surface of the hot-rolled AZ31 plate with high concentrations of {$10\bar{1}0$} and {$10\bar{2}0$} planes shows a larger corrosion rate (about 2 times) than the rolled surface, which mainly contains the (0001) planes [61]. The corrosion rate of the surface parallel to the extrusion direction of the {0002}, {$10\bar{1}0$}, and {$11\bar{2}0$} planes is 3.5 times bigger than that of the surface perpendicular to the extrusion direction with the {$10\bar{1}0$} and {$10\bar{2}0$} planes of the AZ31 bar [62]. The effects of the crystallographic orientation on the corrosion resistance is related to the closely and loosely packed atomic plane, namely the atom density [31]. Because of to higher atomic coordination and stronger bonding, the order of corrosion resistance is almost the same as that of the atomic densities, i.e., the closely packed plane (i.e., {0002} basal plane) showing a smaller corrosion rate [63]. Moreover, the {0002} basal plane with larger atom packing densities results in higher stability of the oxidized film than the non-basal plane [64]. Hagihara et al. have found that the corrosion rates increase in the order $(0001) < (11\bar{2}0) < (10\bar{1}0) < (11\bar{2}3) < (10\bar{1}2)$ and the galvanic current densities follow the order of $(11\bar{2}0)/(10\bar{1}0) < (0001)/(10\bar{1}0) < (11\bar{2}3)/(10\bar{1}2) < (0001)/(11\bar{2}3) < (0001)/(10\bar{1}2)$ in single-crystal Mg and a similar corrosion tendency has been observed from the Mg–Al and Mg–Cu systems [63].

In this study, there are strong basal texture in the STA samples and corrosion anisotropy between the plane RD-TD and plane ND-TD/ND-RD. In contrast, there are

three texture components of the basal poles, one component with <0002> //RD, one with <0002> //TD, and one with <0002>/ND. Obviously, the crystallographic orientation is more uniform in the three dimensions of the TD, RD, and ND thereby reducing the corrosion anisotropy induced by the preferred distribution of the crystallographic orientations.

Generally, grain refinement often reduces the corrosion rate of magnesium alloys [65] because it acts as a physical barrier against corrosion, accelerates formation of the protective layer, and mitigates oxide cracking [66]. The coherent twin boundary is quite effective with respect to grain refinement but the effects of the twin boundary on the corrosion rate is different from that of the grain boundary. Grain refinement in Mg alloys by grain boundaries often hardly vary the grain orientations, whereas that by the $\{10\bar{1}2\}$ twin boundary rotates the (0002) poles by approximately 86°. Because the different crystallographic planes are corroded at different rates, the corrosion rate may increase or decrease depending on the surface as demonstrated by the present study. Compared to the corrosion rate of the STA samples, the corrosion rate of the plane RD-TD of the PDA samples decreases, whereas those of the plane ND-TD and plane ND-RD of the PDA samples increase. In the STA samples, the plane ND-TD and plane ND-RD exhibit smaller corrosion rates than the plane RD-TD. With regard to the PDA samples, rotation of the crystallographic planes by the $\{10\bar{1}2\}$ twins lead to the inclusion a portion of the plane ND-TD or plane ND-RD in the plane RD-TD and inclusion a part of the plane RD-TD in the plane ND-TD or plane ND-RD. It produces a smaller corrosion rate for the surface ND in the PDA samples than STA samples, but a bigger corrosion rate for the plane ND-TD and plane ND-RD of the PDA samples than the STA samples. Wang et al. [62] have mentioned that the different crystallographic orientations between the matrix and twins promote galvanic corrosion between the twinned and untwined zones.

Moreover, grain boundaries could act as physical barriers for corrosion of Mg alloys, the corrosion rate of fine-grains is often lower than that of the coarse-grains [67]. Similar to grain boundaries, twin boundaries (TBs) are also effective barriers to corrosion attack. However, the influence of twins on corrosion resistance of Mg alloys is still in debate. For example, some studies reported that twins could accelerate the corrosion rate by intra-granular corrosion [68], while other studies reported that the extension twins could enhance corrosion resistance, because it could contribute to the formation of homogeneous oxide film in twinned regions [69]. Wang et al. [70] have reported that the dense twins could be considered as an effective way for improving corrosion resistance and enable re-distribution of crystallographic orientations for weakening corrosion anisotropy. In this work, the dual twin structures are prepared and generate more uniform crystallographic orientations, which could reduce the corrosion anisotropy and improve corrosion resistance. Li et al. [71] have reported that the uniform distribution and morphology of fine precipitations can improve the corrosion resistance of ZK60 alloy. Compared to STA samples, the uniform distribution of the finer disk-shape β″ phases could improve the corrosion resistance of the PDA samples. Based on the description mentioned above, the main mechanism for the lower corrosion anisotropy of the PDA samples is ascribed to the uniform crystallographic orientations generated by the dual twin structure.

5 Conclusion

A new biomedical Mg–6Zn–0.5Zr alloy containing a large number of twins is prepared by cross compression to reduce the strong mechanical and corrosion anisotropy, which make it a desirable candidate as biodegradable implants. The microstructure, mechanical properties, and corrosion behavior are assessed systematically. The dual twin structure not only improves the strength without compromising the ductility, but also removes the tension–compression yield asymmetry along the RD, TD, and ND completely. The CYS/TYS or TYS/CYS ratios of the PDA samples are 0.98 along the RD, 0.99 along the ND, and 0.99 along the TD in comparison with 0.62 along the RD, 0.81 along the ND, and 0.83 along the TD for the STA samples. The mechanism for the reduced tension–compression yield asymmetry is understand as that multiple deformation modes (two or three types) were pre-dominated during both tension and compression attributed to the coexist of different types of twins. The corrosion anisotropy of the plane RD-TD, plane ND-TD, and plane ND-RD is reduced, for example, 1.6 times between the largest corrosion rate (plane RD-TD) and smallest one (plane ND-TD) for the STA samples compared to 1.2 times for the PDA samples. The twins rearrange the crystallographic planes along the RD, TD, and ND and generate more uniform crystallographic orientations in three dimensions consequently reducing the effects of different crystallographic planes on the corrosion anisotropy of the textured samples.

Acknowledgements The study was supported by the National Natural Science Foundation of China (Nos. 52101132, 51871032 and 51901202), the Natural Science Foundation of Jiangsu Province (No. BK20202010), the Basic and Applied Basic Research Project of Guangzhou (202201011250), and the City University of Hong Kong Strategic Research Grant (No. 7005264).

Declarations

Conflict of interest The authors state that there are no conflicts of interest to disclose.

References

[1] J.X. Chen, X.Y. Zhu, L.L. Tan, K. Yang, X.P. Su, Acta Metall. Sin. -Engl. Lett. **34**, 205 (2020)
[2] P. Trumbo, S. Schlicker, A.A. Yates, M. Poos, J. Am. Diet. Assoc. **102**, 1621 (2002)
[3] L. Zhang, Y. Zhang, J. Zhang, R. Zhao, J. Zhang, C. Xu, Acta Metall. Sin. -Engl. Lett. **33**, 500 (2020)
[4] Y. Shao, R.C. Zeng, S.Q. Li, L.Y. Cui, Y.H. Zou, S.K. Guan, Y.F. Zheng, Acta Metall. Sin. -Engl. Lett. **33**, 615 (2020)
[5] F. Witte, J. Fischer, J. Nellesen, H.A. Crostack, V. Kaese, A. Pisch, F. Beckmann, H. Windhagen, Biomaterials **27**, 1013 (2006)
[6] H. Zreiqat, C.R. Howlett, A. Zannettino, P. Evans, G. Schulze-Tanzil, C. Knabe, M. Shakibaei, J. Biomed. Mater. Res. Part A **62**, 175 (2002)
[7] G. Song, A. Atrens, D.S. John, X. Wu, J. Nairn, Corros. Sci. **39**, 1981 (1997)
[8] Y.F. Zheng, X.N. Gu, F. Witte, Mater. Sci. Eng. R **77**, 1 (2014)
[9] F. Witte, Acta Biomater. **23**(Suppl), 28 (2015)
[10] J.W. Choi, Y.M. Kong, H.E. Kim, I.S. Lee, J. Am. Ceram. Soc. **81**, 1742 (1998)
[11] M.P. Staiger, A.M. Pietak, J. Huadmai, G. Dias, Biomaterials **27**, 1728 (2006)
[12] A. Purnama, H. Hermawan, J. Couet, D. Mantovani, Acta Biomater. **6**, 1800 (2010)
[13] J. Chen, L. Tan, X. Yu, I.P. Etim, M. Ibrahim, K. Yang, J. Mech. Behav. Biomed. Mater. **87**, 68 (2018)
[14] F. Fereshteh-Saniee, N. Fakhar, F. Karami, R. Mahmudi, Mater. Sci. Eng. A **673**, 450 (2016)
[15] Z. Li, X. Gu, S. Lou, Y. Zheng, Biomaterials **29**, 1329 (2008)
[16] S.E. Harandi, M. Hasbullah Idris, H. Jafari, Mater. Des. **32**, 2596 (2011)
[17] C. Yan, Y. Xin, C. Wang, H. Liu, Q. Liu, J. Mater. Sci. Technol. **52**, 89 (2020)
[18] E.A. Lukyanova, N.S. Martynenko, I. Shakhova, A.N. Belyakov, L.L. Rokhlin, S.V. Dobatkin, Y.Z. Estrin, Mater. Lett. **170**, 5 (2016)
[19] Y. Tian, H. Huang, G. Yuan, W. Ding, J. Alloys Compd. **626**, 42 (2015)
[20] A. Singh, H. Somekawa, T. Mukai, Scr. Mater. **56**, 935 (2007)
[21] P. Zhang, Y. Xin, L. Zhang, S. Pan, Q. Liu, J. Mater. Sci. Technol. **41**, 98 (2019)
[22] Y. Chino, K. Kimura, M. Hakamada, M. Mabuchi, Mater. Sci. Eng. A **485**, 311 (2008)
[23] C. Yan, Y. Xin, X.B. Chen, D. Xu, P.K. Chu, C. Liu, B. Guan, X. Huang, Q. Liu, Nat. Commun. **12**, 4616 (2021)
[24] N. Stanford, J. Geng, Y.B. Chun, C.H.J. Davies, J.F. Nie, M.R. Barnett, Acta Mater. **60**, 218 (2012)
[25] Y. Xin, X. Zhou, Q. Liu, Mater. Sci. Eng. A **567**, 9 (2013)
[26] B. Guan, Y. Xin, X. Huang, P. Wu, Q. Liu, Acta Mater. **173**, 142 (2019)
[27] H.H. Yu, C.Z. Li, Y.C. Xin, A. Chapuis, X.X. Huang, Q. Liu, Acta Mater. **128**, 313 (2017)
[28] J. Wang, X. Li, P. Jin, S. Li, G. Ma, L. Zhao, Mater. Res. Express. **5**, 116518 (2018)
[29] A.E. Davis, J.D. Robson, M. Turski, Acta Mater. **158**, 1 (2018)
[30] D.L. Yin, J.T. Wang, J.Q. Liu, X. Zhao, J. Alloys Compd. **478**, 789 (2009)
[31] G.L. Song, R. Mishra, Z. Xu, Electrochem. Commun. **12**, 1009 (2010)
[32] Q. Jiang, X. Ma, K. Zhang, Y. Li, X. Li, Y. Li, M. Ma, B. Hou, J. Magnes. Alloy. **3**, 309 (2015)
[33] Q.H. Zang, H.M. Chen, J. Zhang, J.H. Cho, Y.X. Jin, Y.K. Shi, Mater. Res. Innov. **19**, 102 (2015)
[34] Y. Song, E.H. Han, D. Shan, C.D. Yim, B.S. You, Corros. Sci. **65**, 322 (2012)
[35] X. Lin, L. Tan, Q. Wang, G. Zhang, B. Zhang, K. Yang, Mater. Sci. Eng. C Mater. Biol. Appl. **33**, 3881 (2013)
[36] Z.R. Qi, Q. Zhang, L.L. Tan, X. Lin, Y. Yin, X.L. Wang, K. Yang, Y. Wang, J. Biomed. Mater. Res. A **102**, 1255 (2014)
[37] S. Zhang, Y. Bi, J. Li, Z. Wang, J. Yan, J. Song, H. Sheng, H. Guo, Y. Li, Bioact. Mater. **2**, 53 (2017)
[38] D. Orlov, G. Raab, T.T. Lamark, M. Popov, Y. Estrin, Acta Mater. **59**, 375 (2011)
[39] M. Pérez-Prado, O.A. Ruano, Scr. Mater. **46**, 149 (2002)
[40] H. Chen, T. Liu, Y. Zhang, B. Song, D. Hou, F. Pan, Mater. Sci. Eng. A **652**, 167 (2016)
[41] X. Gao, J.F. Nie, Scr. Mater. **56**, 645 (2007)
[42] Y. Xin, K. Huo, T. Hu, G. Tang, P.K. Chu, J. Mater. Res. **24**, 2711 (2011)
[43] Z. Cui, F. Ge, Y. Lin, L. Wang, L. Lei, H. Tian, M. Yu, X. Wang, Electrochim. Acta **278**, 421 (2018)
[44] Y. Zhang, C. Yan, F. Wang, W. Li, Corros. Sci. **47**, 2816 (2005)
[45] J. Li, B. Zhang, Q. Wei, N. Wang, B. Hou, Electrochim. Acta **238**, 156 (2017)
[46] G. Baril, N. Pébère, Corros. Sci. **43**, 471 (2001)
[47] T. Zhang, G. Meng, Y. Shao, Z. Cui, F. Wang, Corros. Sci. **53**, 2934 (2011)
[48] J. Chen, J. Wang, E. Han, J. Dong, W. Ke, Electrochim. Acta **52**, 3299 (2007)
[49] C.N. Cao, J.Q. Zhang, *An introduction to electrochemical impedance spectroscopy* (Science Press, Beijing, 2002), pp.2l–24
[50] Y. Xin, T. Hu, P.K. Chu, Corros. Sci. **53**, 1522 (2011)
[51] Y. Song, D. Shan, R. Chen, E.H. Han, Corros. Sci. **51**, 1087 (2009)
[52] S. Agnew, D. Brown, C. Tome, Acta Mater. **54**, 4841 (2006)
[53] J. Koike, R. Ohyama, Acta Mater. **53**, 1963 (2005)
[54] L. Wang, Z. Huang, H. Wang, A. Maldar, S. Yi, J.S. Park, P. Kenesei, E. Lilleodden, X. Zeng, Acta Mater. **155**, 138 (2018)
[55] H. Yu, Y. Xin, M. Wang, Q. Liu, J. Mater. Sci. Technol. **34**, 248 (2018)
[56] X. Lou, M. Li, R. Boger, S. Agnew, R. Wagoner, Int. J. Plast. **23**, 44 (2007)
[57] L. Wu, S.R. Agnew, D.W. Brown, G.M. Stoica, B. Clausen, A. Jain, D.E. Fielden, P.K. Liaw, Acta Mater. **56**, 3699 (2008)
[58] H.H. Yu, Y.C. Xin, A. Chapuis, X.X. Huang, R.L. Xin, Q. Liu, Sci. Rep. **6**, 29283 (2016)
[59] Y. Xin, M. Wang, Z. Zeng, M. Nie, Q. Liu, Scr. Mater. **66**, 25 (2012)
[60] B. Song, R. Xin, N. Guo, J. Xu, L. Sun, Q. Liu, Mater. Sci. Eng. A **639**, 724 (2015)
[61] G.L. Song, JOM **64**, 671 (2012)
[62] B.J. Wang, D.K. Xu, J.H. Dong, W. Ke, Scr. Mater. **88**, 5 (2014)
[63] K. Hagihara, M. Okubo, M. Yamasaki, T. Nakano, Corros. Sci. **109**, 68 (2016)
[64] H. Jia, X. Feng, Y. Yang, J. Mater. Sci. Technol. **34**, 1229 (2018)
[65] C. op't Hoog, N. Birbilis, Y. Estrin, Adv. Eng. Mater. **10,** 579 (2008)
[66] D. Ahmadkhaniha, M. Fedel, M. Heydarzadeh Sohi, F. Deflorian, Surf. Eng. Appl. Electrochem. **53**, 439 (2017)
[67] H.S. Kim, G.H. Kim, H. Kim, W.J. Kim, Corros. Sci. **74**, 139 (2013)
[68] N.N. Aung, W. Zhou, Corros. Sci. **52**, 589 (2010)

[69] G. Zou, Q. Peng, Y. Wang, B. Liu, J. Alloys Compd. **618**, 44 (2015)
[70] B.J. Wang, D.K. Xu, Y.C. Xin, L.Y. Sheng, E.H. Han, Sci. Rep. **7**, 16014 (2017)
[71] X. Li, J.H. Jiang, Y.H. Zhao, A.B. Ma, D.J. Wen, Y.T. Zhu, Trans. Nonferrous Met. Soc. China **25**, 3909 (2015)